

Beam geometry, alignment, and wavefront aberration effects on interferometric differential wavefront sensing

This content has been downloaded from IOPscience. Please scroll down to see the full text.

2015 Meas. Sci. Technol. 26 125203

(<http://iopscience.iop.org/0957-0233/26/12/125203>)

View [the table of contents for this issue](#), or go to the [journal homepage](#) for more

Download details:

IP Address: 81.31.147.91

This content was downloaded on 28/06/2016 at 01:51

Please note that [terms and conditions apply](#).

Beam geometry, alignment, and wavefront aberration effects on interferometric differential wavefront sensing

Xiangzhi Yu¹, S R Gillmer¹ and J D Ellis^{1,2}

¹ Department of Mechanical Engineering, University of Rochester, Rochester, NY 14627, USA

² The Institute of Optics, University of Rochester, Rochester, NY 14627, USA

E-mail: xiangzhi.yu@rochester.edu

Received 20 July 2015, revised 29 September 2015

Accepted for publication 5 October 2015

Published 27 October 2015



Abstract

Heterodyne interferometry is a widely accepted methodology with high resolution in many metrology applications. As a functionality enhancement, differential wavefront sensing (DWS) enables simultaneous measurement of displacement, pitch, and yaw using a displacement interferometry system and a single beam incident on a plane mirror target. The angular change is measured using a weighted phase average between symmetrically adjacent quadrant photodiode pairs. In this paper, we present an analytical model to predict the scaling of differential phase signals based on fundamental Gaussian beams. Several numerical models are presented to discuss the effects of physical beam parameters, detector size, system alignment errors, and beam wavefront aberrations on the DWS technique. The results of our modeling predict rotational scaling factors and a usable linear range. Furthermore, experimental results show the analytically predicted scaling factor is in good agreement with empirical calibration. Our three degree-of-freedom interferometer can achieve a resolution of 0.4 nm in displacement and 0.2 μ rad in pitch and yaw simultaneously.

Keywords: interferometry, metrological instrumentation, optical metrology, stage calibration

(Some figures may appear in colour only in the online journal)

1. Introduction

Heterodyne interferometry is an essential method in many industrial metrology applications due to its high dynamic range, high signal-to-noise ratio, and direct traceability to length standards [1, 2]. Displacement interferometers with sub-nanometer resolution and nanometer-level uncertainty are readily achievable by adopting a sufficiently frequency stabilized laser source and a strictly controlled environment [3, 4]. Several types of interferometer configurations have been proposed to further improve the resolution and change functional parameters (e.g. [5–10]). Most heterodyne angular interferometers are based on total internal reflection [11, 12] or a measured optical path difference (OPD) from rotation in a Michelson interferometer-based configuration [13–15]. Although high resolution has been achieved in linear and rotational displacements independently, limitations still exist

in the measurement of multiple degrees of freedom (DOF) simultaneously. Furthermore, most interferometry systems utilize larger targets when measuring angles, thereby adding mass to the measurement system which alters the dynamic performance by lowering natural frequencies and decreasing translational bandwidth.

In this paper, we present a simple method for simultaneous three-DOF interferometric measurements. The methodology is suitable for applications in machine tool metrology. Although our discussed sensor can be empirically calibrated, this calibration factor will change when the setup is moved to separate measurement sites. Therefore, we have established an analytical model which will predict rotational scaling factors from measurements of the two interfering beam wavefronts using a Shack–Hartmann wavefront sensor. The predicted scaling factor differs from empirical calibration by 1%.

Differential wavefront sensing (DWS) is a relatively new technology with a growing variety of applications, mainly in the area of optical alignment [16–19]. The New Gravitational wave Observatory (NGO—formerly the Laser Interferometer Space Antenna—LISA) project, which is a proposed space mission concept designed to detect and accurately measure gravitational waves, has applied DWS to monitor and track the longitudinal motion and attitude of two floating test masses with precision in the picometer and nanoradian range, respectively [20–23]. Within that project, a three DOF metrology package using DWS has been outlined and characterized [24, 25]. Analytical models and simulations have been developed to describe DWS where the beam diameters are much smaller than the detector size [26, 27]. The high levels of performance were achieved using empirical calibration; however, the agreement with analytical models differed by up to 10% [23]. This manuscript demonstrates that similar analytical modeling incorporating beam wavefront aberrations and misalignment provides a $10 \times$ improvement in the agreement of analytically predicted and empirically calibrated performance. Our proposed sensor can be readily implemented for machine tool calibrations with improved performance compared to the commercially available XD6TM API laser measurement system. Furthermore, this three DOF sensor offers comparable performance to alternative approaches with a more simplified approach [28–31].

In previous work [23, 26, 27], it was assumed that the beam size was much smaller than the quadrant detector overall area. The smaller beam size, however, could lead to spatial inhomogeneity issues in the photodiode quadrants as beam centroids translate in response to a measured rotation. Gillmer *et al* [32] developed a modified Joo-type interferometer as a compact, fiber-coupled three DOF interferometer, which simultaneously measures displacement along with changes in pitch and yaw using a single optical beam incident on a small plane mirror target. In that work, the quadrant photodetector area was overfilled, thereby rendering individual detector inhomogeneities and gaps in the overall area negligible. In this paper, we generalize the physical model presented by Gillmer *et al* for arbitrary beam and detector sizes based on fundamental Gaussian parameters. Additionally, various system alignment errors are considered in the model for DWS simulations. Finally, different beam wavefront aberrations are investigated for their effects on the sensitivity of DWS signals.

2. Interferometer operating principle

2.1. Three DOF interferometer

The compact, fiber-delivered three DOF interferometer is shown in figure 1. The light from a stabilized laser source (633 nm) is split equally and directed towards two acoustic-optic modulators (AOMs). The two AOMs are driven at slightly different RF frequencies to create a frequency difference between the two beams, which results in a carrier heterodyne frequency after interference occurs. After the AOMs, the first orders of the two modulated beams are individually fiber-coupled into polarization maintaining fibers and then

collimated back into free space. The f_1 beam passes through the top non-polarizing beamsplitter (BS), reflects from the fixed reference surface and interferes with the f_2 beam that is reflected from the bottom BS. Likewise, the f_2 beam passes through the bottom BS, reflects from the measurement mirror target on the stage, and interferes back at the bottom BS with the f_1 beam that is reflected from the top BS. The information for displacement, pitch, and yaw can be decoupled from the phase difference between the measurement quadrant photodetector and the reference photodetector using DWS.

2.2. Differential phase signals

Differential wavefront sensing utilizes a quadrant photodetector as the measurement detector, and the individual phase change at each quadrant relative to the reference photodetector is detected and computed from the interference wavefront. The phase shift will be the same for all four quadrants if only translation occurs. Thus, the overall stage displacement is determined by averaging the measured phase between all quadrants. However, the phase shift is different from quadrant to quadrant if there is angular change between the two wavefronts, such as the pitch indicated in figure 2. Thus, by creating a weighted phase average over symmetrically adjacent quadrant detector pairs, the pitch and yaw results can be decoupled from DWS signals. The three DOFs are demodulated according to

$$z \propto \frac{\phi_A + \phi_B + \phi_C + \phi_D}{4}, \quad (1)$$

$$\text{pitch} \propto \frac{(\phi_A + \phi_B) - (\phi_C + \phi_D)}{L_p}, \quad (2)$$

and

$$\text{yaw} \propto \frac{(\phi_A + \phi_C) - (\phi_B + \phi_D)}{L_y}, \quad (3)$$

where ϕ represents detected phase of quadrant A, B, C or D. Here $L_p = 2h/S_p$ and $L_y = 2w/S_y$, where $2h$ and $2w$ are the physical dimensions of the quadrant photodetector (see figure 2), L_p and L_y represent an equivalent length in pitch and yaw measurements that is primarily dependent on beam diameter, detector size, alignment errors, and beam wavefront, and variables S_p and S_y are scaling factors to determine the equivalent length for pitch and yaw, respectively. Generally, a larger equivalent length increases the measurement sensitivity because the distance between the two effective measurement points is greater. While symmetric beams and detectors yield equivalent values for L_p and L_y , in practice, misalignment and aberrations will cause subtle variations that affect the pitch and yaw angular sensitivities independently.

3. DWS analytical model

The basic model and procedure are first proposed in [27] to simulate DWS signals. In this section, we provide a revised model based on realistic (aberrated) beam parameters and

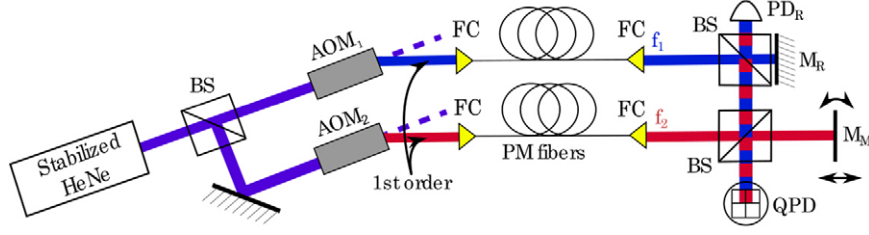


Figure 1. Schematic of the fiber coupled, three DOF interferometer. (BS: beam splitter, AOM: acousto-optic modulator, FC: fiber coupler, PD: photodetector, M: mirror, QPD: quadrant photodetector).

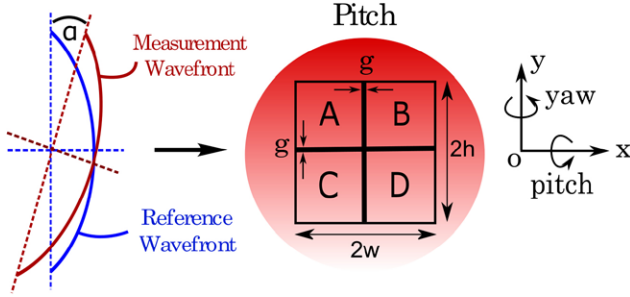


Figure 2. Schematic of a rectangular quadrant photodetector for differential wavefront sensing with a tilted measurement wavefront. The quadrants are labeled A through D.

identify a coordinate space for misalignment. Each electric field incident on the quadrant detector is assumed to be a fundamental-order Gaussian,

$$E(r) = |E| \frac{\omega_0}{\omega(z)} e^{-\frac{r^2}{\omega(z)^2} - ik \frac{r^2}{2R(z)} - ikz + i\zeta(z) + i\omega t}, \quad (4)$$

where r is the distance from the origin, z is the axial distance from the beam waist, ω_0 is the waist size, λ is the wavelength, k is the wave number, $\omega(z) = \omega_0 \sqrt{1 + (z/z_R)^2}$ is the beam waist, $R(z) = z [1 + (z_R/z)^2]$ is the radius of curvature of the wavefront, $\zeta(z) = \arctan(z/z_R)$ is the Gouy phase shift, and $z_R = \pi \omega_0^2 / \lambda$ is the Rayleigh range. Since the quadrant photodetector is square, it is more convenient to describe the two beams in Cartesian coordinates. The expressions for reference and measurement beams, respectively, are

$$E_1(x, y) = |E_1| \frac{\omega_{0,1}}{\omega(z_1)} e^{-\frac{x^2 + y^2}{\omega(z_1)^2} - i \left[k \frac{x^2 + y^2}{2R(z_1)} + kz_1 - \zeta(z_1) - \omega_1 t \right]}, \quad (5)$$

$$E_2(x, y) = |E_2| \frac{\omega_{0,2}}{\omega(z_2)} e^{-\frac{(x-\delta x)^2 + (y-\delta y)^2}{\omega(z_2)^2} - ik \frac{(x-\delta x)^2 + (y-\delta y)^2}{2R(z_2)} + i\omega_2 t} e^{-ikz_2 + i\zeta(z_2) - i\phi_m - ik[2\beta(x-\delta x) + 2\alpha(y-\delta y)]}. \quad (6)$$

In this analytical model, the origin of the Cartesian coordinates is at the center of the quadrant photodetector, where the X-direction is along the horizontal direction, the Y-direction is along the vertical direction. The reference beam centroid is assumed to coincide with the detector center. For the measurement beam expression, α is the angular rotation about the X-axis (pitch), β is the angular rotation about Y-axis (yaw), δx and δy are the beam centroid coordinates compared to the reference beam centroid, ϕ_m is an extra phase shift from beam

wavefront aberrations. In the simplified analytical model, we assume a fundamental-order Gaussian beam, which means ϕ_m is zero when there are no aberrations present.

The two interfering beams are incident on the quadrant photodetector, and the measured irradiance is proportional to the modulus squared of the electric field,

$$I(x, y) \propto |E_1(x, y) + E_2(x, y)|^2. \quad (7)$$

For the quadrant photodetector, the resulting optical power in each quadrant, for example quadrant A, is the irradiance integrated over the detector area,

$$A \propto \int_{-g/2}^{-g/2} \int_{g/2}^{g/2} I(x, y) dx dy, \quad (8)$$

where g is the width of detector gap. Assuming lock-in detection to demodulate the heterodyne signals [33], the D.C. components are filtered and we only focus on the interference term which has the form,

$$A = f_A(z, \alpha, \beta) e^{i\omega_1 t} + f_A^*(z, \alpha, \beta) e^{-i\omega_1 t}. \quad (9)$$

We process equation (9) to extract the in-phase component, I_A , and quadrature component, Q_A . Thus, the phase change for quadrant A can be calculated using

$$\phi_A = \arctan \left\{ \frac{Q_A}{I_A} \right\}. \quad (10)$$

Similarly, the output signals for the other three quadrants B, C and D are determined by changing the limits of integration according to the individual dimension coordinates and applying the same post processing procedure to determine ϕ_B , ϕ_C , and ϕ_D , respectively.

4. Simulations for different beam and detector sizes

The beam and detector sizes are two main parameters that will affect the final DWS signals. Numerical simulations were performed to investigate their effects on the angular sensitivity. The full mathematical expressions for the analytical model are used in the simulations and the two beams are assumed to have ideal alignment. In addition, the responsivity for the four quadrants of quadrant photodetector (QPD) are assumed to be equal.

In practice, there is gap (assumed a 100 μm wide, cross-shaped area) between the four channels in the quadrant photodiode. Thus, the integration limits do not start from zero but rather from 50 μm in the simulations. The distance between the measurement mirror and QPD is 150 mm, the axial distance

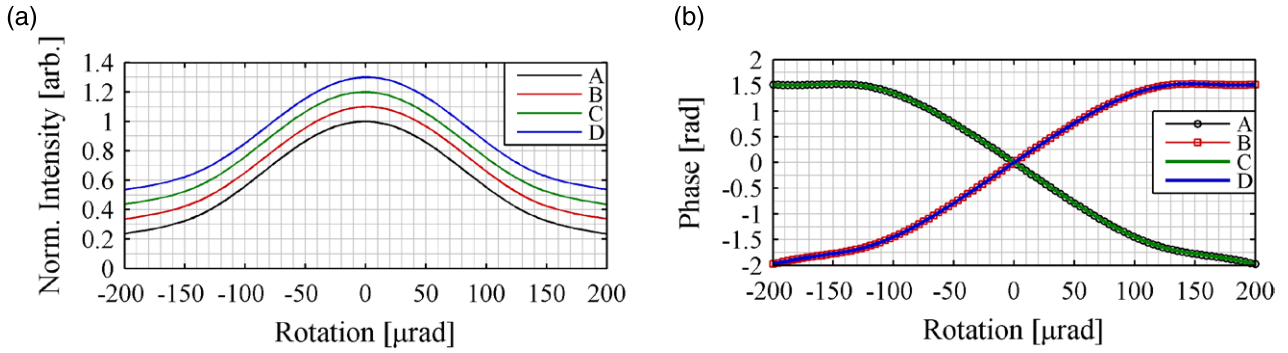


Figure 3. (a) Normalized intensity and (b) phase change with the mirror rotating from -200 to $200 \mu\text{rad}$ for the four quadrants A, B, C and D. In (a), A is the true value while B, C, and D are each offset by 0.1 for clarity.

z_1 and z_2 are both 400 mm , and the measurement beam center shift caused by mirror rotation is considered. Because the pitch and yaw are two orthogonal and symmetrical rotations about their respective axis, in the simulations we only discuss the yaw rotation. In the first simulation, both measurement and reference beam diameters were set at 4 mm ($\omega_0 = 2 \text{ mm}$) and the photodiode quadrants are a 5 mm by 5 mm square. The angular change was simulated with yaw rotation from $-200 \mu\text{rad}$ to $200 \mu\text{rad}$. Figure 3 shows the resulting intensity and phase change for the four quadrants during the rotation. The individual phase change can be converted to displacement information by,

$$z = \frac{\phi \lambda}{2\pi n N}, \quad (11)$$

where $\lambda (=633 \text{ nm})$ is the wavelength of the laser, $N = 2$ is the interferometer fold constant, n is the refractive index. After converting four phase change values (ϕ_A , ϕ_B , ϕ_C , and ϕ_D) to four displacements values at (z_A , z_B , z_C , z_D) on the four quadrants, the theoretical yaw rotation is calculated as

$$\beta = \frac{(z_A + z_C) - (z_B + z_D)}{2w}. \quad (12)$$

As shown in figure 4, the theoretically calculated yaw rotation is a globally nonlinear curve but includes a linear section in the center. The nonlinear curve could be represented by a high-order polynomial. However, we are more interested in the linear portion which shows the sensitivity of the measurement and is immune to offsets (which is critical during the presence of aberrations). We define the linear range here as the maximum rotation range that ensures the error between our theoretical rotation and ideal straight yaw rotation is within $1 \mu\text{rad}$. This is an index to estimate the working range for rotation and depends on different system and beam parameters. The linear range is valid and useful for DWS, so we only focus on this range and scale it to match the ideal result. We define this number as scaling factor, S_p or S_y , used to calculate equivalent length which will eventually determine the final yaw rotation. In this simulation, the scaling factor is 1.5932 , the equivalent length is 3.1384 mm and the linear range is from -59 to $59 \mu\text{rad}$, which ensures the error between theoretical yaw rotation and the ideal yaw rotation is within $1 \mu\text{rad}$ (figure 4).

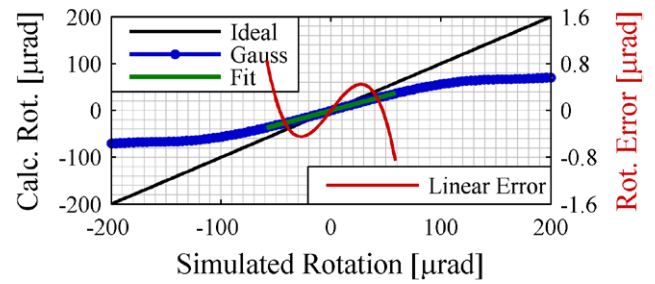


Figure 4. The comparison between the theoretical calculated rotation for 4 mm diameter beam and the ideal result (plane wavefront with uniform intensity distribution) within the simulated rotation from -200 to $200 \mu\text{rad}$ and scaled linear range.

The nonlinearity is a result of interfering Gaussian beams. As shown in figure 4, when plane waves are considered (ideal case) no such nonlinearity is present. There are three main factors that cause this nonlinearity. First, the gap between the four elements of QDP causes some nonlinearity. Second, the measurement beam center shifts during the rotation. The last and the most important explanation is there will be destructive interference in wavefronts across parts of the QPD when the rotation is large. Figure 5 demonstrates that when the rotation is relatively small as shown by θ_1 , the phase difference between two wavefronts along the detector center line remains within one spatial fringe. However, when there is excessive rotation, as depicted by θ_2 , there will be phase jumps within the detector area that will degrade signal quality.

Beam diameter and detector size were investigated to determine their effect on the theoretical rotation. The beam diameter was kept constant at 4 mm ($\omega_0 = 2 \text{ mm}$) and three simulations were performed for different square QPD sizes with edge sizes of 3 mm , 5 mm , and 7 mm . In addition, the QPD size was kept constant at 5 mm by 5 mm and three simulations were performed for different beam diameters of 2 mm , 4 mm , and 6 mm . The results are shown in figure 6. For the purposes of calculating the equivalent length and linear range, the maximum angular error is assumed to be $< 1 \mu\text{rad}$.

It is clear that the equivalent length and linear range (error within $1 \mu\text{rad}$) are determined by the beam size and QPD dimensions. Generally, larger beam diameters increase sensitivity and smaller detector sizes increase the linear range. Simulation maps were generated for beam diameters from 2 to 6 mm and QPD dimensions from a 3 mm square

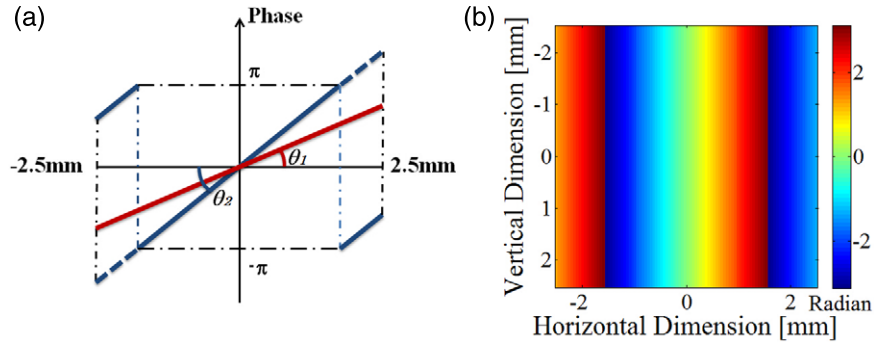


Figure 5. The left plot shows the comparison between the phase changes for different rotations along the detector center line. The right plot shows the phase map over the detector area for a relatively large rotation.

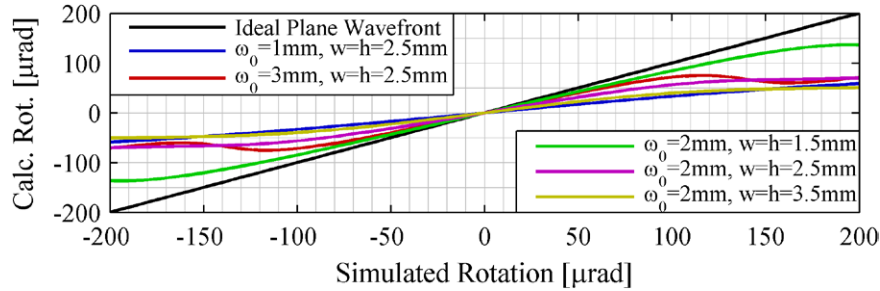


Figure 6. The theoretical calculated rotation for beam with 4 mm diameter ($\omega_0 \omega_0 = 2$ mm) in different QPD dimensions ($w = h = 1.5$ mm, $w = h = 2.5$ mm, $w = h = 3.5$ mm) and for a certain detector size ($w = h = 2.5$ mm) with different beam sizes ($\omega_0 = 1$ mm, $\omega_0 = 2$ mm, $\omega_0 = 3$ mm) within the simulated rotation from -200 to 200 μ rad.

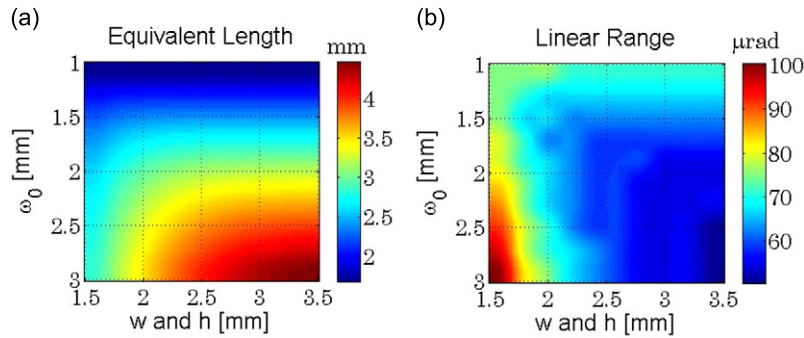


Figure 7. Equivalent length and linear range map for different beam sizes and QPD dimensions. The equivalent length increases (and thus measurement resolution improves) with increasing beam size and detector size. However, the larger detector size negatively influences the linear sensitivity range.

($w = h = 1.5$ mm) to a 7 mm square. The results, shown in figure 7, demonstrate that beams with a larger diameter incident on a smaller QPD will have a larger linear range and a smaller scaling factor. However, the highest sensitivity will occur when the beam diameter and detector size are larger, presenting a tradeoff between sensitivity and linearity.

5. Alignment errors

In practical applications, ensuring perfect beam alignment is not possible. Typically, alignment errors, as shown in figure 8, include beam center mismatch, beam size mismatch, and beam tilt, to name a few. These alignment errors were investigated for their effect on DWS and the scaling factor. As in the previous case, only yaw rotation is considered here, pitch may be incorporated using the same prescribed process.

5.1. Beam center mismatch

The beam center mismatch is in two directions, δx and δy . In this situation, the two beams are parallel to each other and all the other parameters are the same. The beam diameter is 4 mm, the QPD dimensions are 5 mm by 5 mm, the distance between the measurement mirror and QPD is 150 mm, the axial distance z is 400 mm. For the yaw rotation, it is intuitive that δy will not affect the result because of symmetry about Y -axis. Thus, only the beam center mismatch in the X -direction is considered. The δx is from -0.5 to 0.5 mm at the detector and the equivalent length change is shown in figure 9(a). Within this δx range, the yaw rotation linear range is still from -59 to 59 μ rad. Also, the equivalent length is only marginally sensitive to beam center shift, <0.02 mm over the 1 mm shift range. Similarly, pitch rotation will not be affected by δx and the equivalent

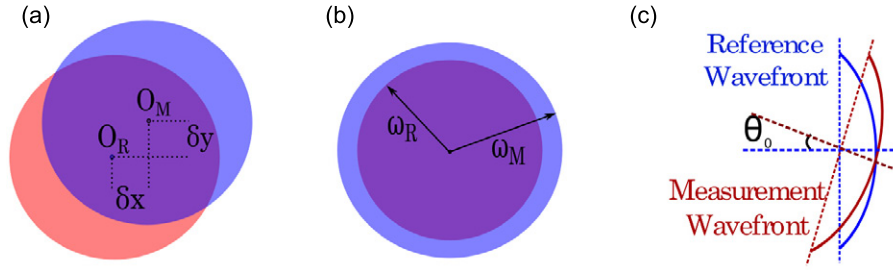


Figure 8. The schematic for different beam misalignments. (a) Beam center mismatch, (b) beam size mismatch, (c) beam tilt.

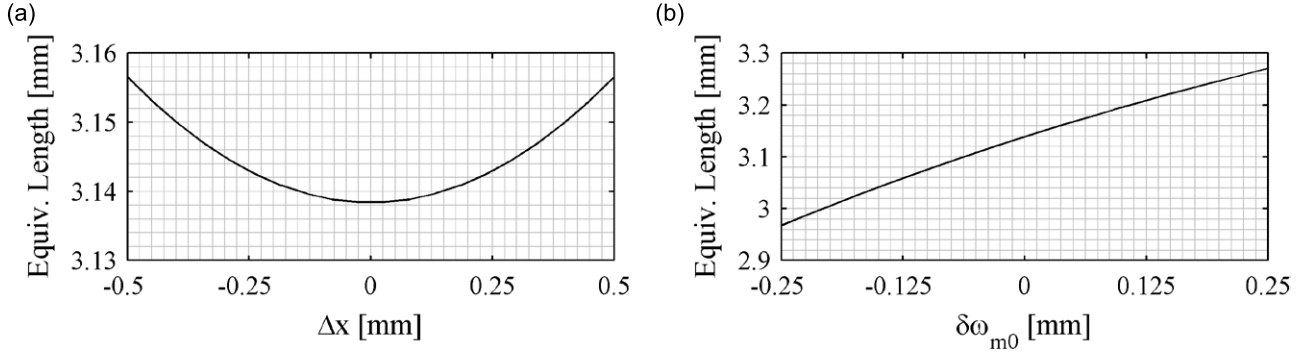


Figure 9. (a) The equivalent length variation for δx from -0.5 mm to 0.5 mm. (b) The equivalent length variation for reference beam diameter at 4 mm ($\omega_{m0} = 2$ mm) but measurement beam diameter from 3.5 to 4.5 mm.

length variation caused by δy will be the same as shown in figure 9(a).

5.2. Beam size mismatch

For the interferometer shown in figure 1, the beams in the interferometer need some form of collimation from the fibers. Because of manufacturing and assembly variability, the waist size of both beams may have a small difference. Here, we assume the reference beam diameter is 4 mm and the measurement beam diameter is changing from 3.5 to 4.5 mm. All the other parameters are maintained and there are no other alignment errors. Figure 9(b) shows the equivalent length variation due to beam diameter mismatch. Within this beam size difference, the linear rotation range is still from -59 to 59 μrad . Here, the equivalent length changes approximately 0.3 mm (from ~ 2.95 mm to ~ 3.25 mm), representing a $\sim 10\%$ change in sensitivity.

5.3. Beam tilt

In the simulations above, the initial angle between the measurement and reference beams is zero, and the DWS signals are used to calculate extra wavefront tilt caused by the measurement mirror rotation. Because of the alignment errors, there might be some initial angle between the two beams and we will investigate how this affects DWS results.

If the initial yaw angle is θ_0 and all the other parameters are kept constant, the shape of the theoretical calculated rotation curve will be the same except the origin shifts to a mirror rotation at $\theta_0/2$ (the mirror rotation θ will cause 2θ for a beam angle change due to reflection). For instance, if the initial

yaw angle is 20 μrad between two beams with 4 mm diameter incidence onto a 5 mm by 5 mm QPD, the scaling factor is still 1.5932 and the equivalent length is 3.1384 mm, while the linear range changes from -69 to 49 μrad . The beam tilt maintains the scaling factor and equivalent length but only changes the linear range.

5.4. Beam alignment summary

Comparing the different alignment effects discussed—beam center mismatch, beam size mismatch, and initial tilt between beams—yields beam size having the largest impact on the equivalent length. Beam size errors are approximately $10 \times$ more sensitive than beam center mismatch. This has implications for two practical reasons: (1) beam sizes can be readily measured and should be nominally constant after the interferometer is established, and (2) beam center position changes, which are less sensitive, change as a function of target mirror angle and distance from the interferometer. Because this effect is less sensitive and depending on the range and/or angular error of the measurement target, certain applications yield effectively a constant equivalent length for which the error is still minimal. However, for greater positioning changes and/or angles, the beam center location should be tracked based on the initial target mirror offset and the equivalent length updated appropriately to improve accuracy. Because we assume a linear proportionality between target mirror angle change and measured signal, the initial beam tilt effects are negated. Otherwise, a more complicated polynomial expression that changes sensitivity as a function of angle must be used.

Table 1. Influences on the equivalent length and linear range for individual aberrations. When the reference beam wavefront has a high quality and interferes with an aberrated measurement beam, there are influences on both. However, when the measurement and reference beams exhibit the same aberrations, the equivalent length and linear range are nominally the same.

Mode j	Classic name	Measurement wavefront aberrated		Measurement and reference wavefronts aberrated	
		Equivalent length (mm)	Linear range (μrad)	Equivalent length (mm)	Linear range (μrad)
4	Astig y	3.1177	−59 to 59	3.1384	−59 to 59
5	Power	3.0858	−59 to 59	3.1260	−59 to 59
6	Astig x	3.1081	−59 to 59	3.1278	−59 to 59
7	Trefoil y	3.1303	−59 to 59	3.1384	−59 to 59
8	Coma y	3.1682	−59 to 59	3.1366	−59 to 59
9	Coma x	3.1332	−22 to 95	3.1366	−59 to 59
10	Trefoil x	3.1313	−63 to 55	3.1366	−59 to 59
11	Tetrafoil y	3.1359	−59 to 59	3.1366	−59 to 59
12	2nd Astig y	3.0210	−59 to 59	3.1366	−59 to 59
13	Spherical	2.8541	−55 to 55	3.1758	−59 to 59
14	2nd Astig x	2.9832	−59 to 59	3.1675	−59 to 59
15	Tetrafoil x	3.1345	−59 to 59	3.1380	−59 to 59

6. Beam aberrations

Modeling the beam as a perfect fundamental-order Gaussian profile may not be accurate enough for DWS in practice. The final beams will have wavefront aberrations due to optical components' manufacturing tolerances and assembly errors. To account for this, we introduce the extra phase shift caused by aberrations in our model.

The Zernike polynomials are useful for describing wave aberration functions over circular pupils with unit radius. Individual terms or modes of a Zernike polynomial are mutually orthogonal over the unit circle and are easily normalized to form an orthonormal basis [34]. They are usually defined in polar coordinates (ρ, θ) , where ρ is the radial coordinate ranging from 0 to 1 and θ is the azimuthal component ranging from 0 to 2π . In general, a double indexing scheme is used for describing the polynomial with the index n describing the highest power or order of the radial polynomial and the index m describing the azimuthal frequency of the azimuthal component as,

$$Z_n^m(\rho, \theta) = N_n^m R_n^{|m|}(\rho) \cos m\theta, \text{ for } m \geq 0, \quad (13)$$

$$Z_n^m(\rho, \theta) = -N_n^m R_n^{|m|}(\rho) \sin m\theta, \text{ for } m < 0, \quad (14)$$

where $R_n^m(\rho)$ is given by,

$$R_n^{|m|}(\rho) = \sum_{s=0}^{(n-|m|)/2} \frac{(-1)^s (n-s)!}{s! [0.5(n+|m|-s)]! [0.5(n-|m|)-s]!} \rho^{n-2s}. \quad (15)$$

And N_n^m is the normalization factor

$$N_n^m = \sqrt{\frac{2(n+1)}{1+\delta_{m0}}}, \quad (16)$$

where δ_{m0} is the Kronecker delta function.

In the numerical model, it is much easier to use the mathematical expression for Zernike polynomials (normalized

by RMS) in Cartesian coordinates and ordering the Zernike mode by a single index j . Thus, the entire wavefront can be expressed in terms of a set of Zernike functions,

$$W(x, y) = \sum_0^{15} c_n Z_n(x, y), \quad (17)$$

where c_n are the Zernike coefficients. The extra phase shift can be calculated using,

$$\varphi(x, y) = \frac{2\pi W(x, y)}{\lambda}. \quad (18)$$

For the first three Zernike polynomials, piston (Z_1) is a constant phase shift for the whole wavefront and will not affect the result. Tip (Z_2) and tilt (Z_3) are basic alignment errors that have already been discussed. Thus, in this section, we only focus on higher order (2nd, 3rd and 4th) aberrations. To investigate their effects, we keep the beam diameter at 4 mm and the QPD dimensions at 5 mm by 5 mm as above as these are readily available for practical applications. When the system is in good alignment, the reference wavefront does not have any aberrations and we only introduce 0.1 μm aberration (pupil size is 10 mm) to each mode for the measurement wavefront. The original scaling factor simulated with a perfect Gaussian beam is 1.5932, the equivalent length is 3.1384 mm, and the linear range is from −59 to 59 μrad .

Table 1 shows how these Zernike polynomials affect DWS results. The results indicate that Z_5 (power), Z_8 (coma y), Z_{12} (2nd astigmatism y), Z_{13} (spherical), Z_{14} (2nd astigmatism x) will affect the scaling factor and equivalent length more than 1%, Z_{10} (trefoil x) and especially Z_9 (coma x) will cause an unbalance for the linear range in positive and negative rotations, Z_{13} (spherical) will also change the linear range slightly but will not affect the symmetry. For precision systems, the aberrations for both wavefronts will likely be close and can be measured. Thus, in the following DWS simulation, we

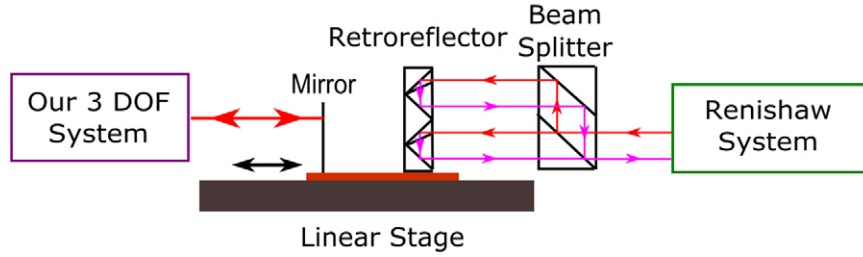


Figure 10. Experimental setup comparing our three DOF interferometer calibration result with Renishaw system for a motorized linear stage.

introduce a $0.1 \mu\text{m}$ aberration (pupil size is 10 mm) to both wavefronts and keep all the other parameters the same.

Table 1 also shows how each Zernike polynomial affects equivalent length and linear range. The results indicate that the linear range will be the same if both wavefronts have the same amount of aberrations. Also, Z_5 (power), Z_6 (astigmatism x), especially Z_{13} (spherical) and Z_{14} (2nd astigmatism x) will contribute a large change in the scaling factor and equivalent length.

In this section, each Zernike polynomial was presented separately to investigate their effects individually. A combination of the Zernike polynomials for a real complex wavefront can also be simulated for DWS if the Zernike coefficients are measured or known.

7. Experimental results

To experimentally validate the theoretical model with aberrations and misaligned beams, we compared the three DOF interferometer from figure 1 with a commercial Renishaw angle interferometer, as shown in figure 10. The two measurement systems calibrate the same motorized linear stage on opposite sides. Our system uses a half inch mirror as the target which gives the displacement, pitch and yaw results simultaneously when the stage is moving. The Renishaw system uses a traditional interferometer with a fixed retroreflector pair as the measurement target and is a widely accepted standard for angle calibrations. Since the Renishaw system can only measure one DOF in a single measurement, we choose the yaw measurement for comparison. In the experiment, the linear stage moves 15 mm in 60 s and the two systems measure the same movement simultaneously from two sides at a 100 Hz sampling frequency to our host PC.

For the three DOF interferometer, an equivalent length is needed to calculate the yaw rotation. The specification of the collimator shows the collimated beam diameter is 3.4 mm and the detector size is 5 mm by 5 mm. In our initial experiment, we assume the beam is a perfect Gaussian beam without any aberrations and the system is in perfect alignment. The simulated equivalent length based on this assumption is 2.6362 mm. Our yaw measurement result is processed based on this equivalent length and the comparison with the Renishaw measurement result is shown in figure 11. These results demonstrate that DWS signals agree with commercial angle interferometers to within 10% which confirms previously reported results [23]. Thus, to improve the accuracy of the DWS signals, more

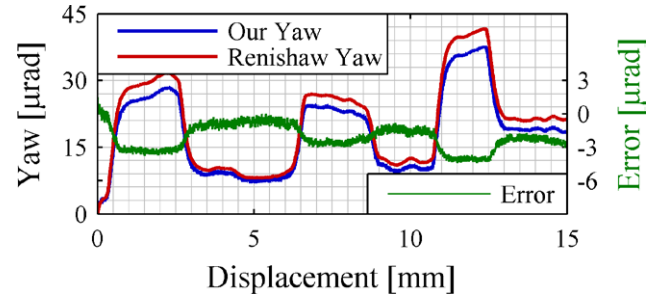


Figure 11. The comparison of yaw measurement during linear motion within 15 mm range processed using a simulated effective length 2.6362 mm based on nominal beam diameter and detector size.

information besides the nominal beam diameter and detector size is needed.

To better predict the equivalent length, a Shack–Hartmann wavefront sensor with a $\lambda/50$ rms wavefront sensitivity was used to measure the beam parameters and aberrations. Figure 12 shows the beam intensity profile captured by the sensor, the beam diameter is a weighted diameter calculated as,

$$\frac{2}{\omega^2} = \frac{1}{\omega_x^2} + \frac{1}{\omega_y^2}, \quad (19)$$

where ω_x is the beam diameter in the X-direction and ω_y is the beam diameter in the Y-direction. Thus, the reference beam diameter is 3.24 mm and the measurement beam diameter is 3.2 mm. In the experiment, we tried to balance the power of the four quadrants to ensure the QPD is placed at the interference beam center, which is the coordinate system origin. The reference beam center is $(-0.013 \text{ mm}, 0.016 \text{ mm})$ and the measurement beam center is $(0.005 \text{ mm}, -0.012 \text{ mm})$. The measured coefficients for the first 15 Zernike polynomials are shown in table 2 based on a 5.411 mm diameter pupil. The simulated equivalent length based on all these measured beam parameters and aberrations is 2.383 mm. Using the aberrated equivalent length, the results show high agreement between both systems (figure 13). The deviation between the two measurement methods yields a $<1\%$ variation ($0.32 \mu\text{rad}/42 \mu\text{rad}$). Thus, incorporating beam aberrations, actual beam size, and beam center mismatch yields a $10 \times$ improvement over traditional DWS models.

In practice, an empirical calibration can be used to determine the equivalent length if the interferometer does not

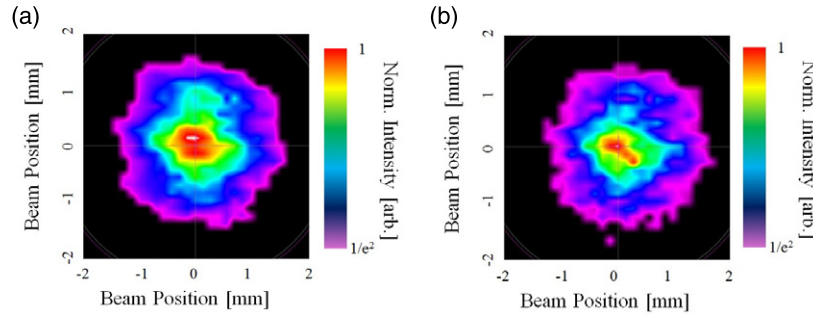


Figure 12. Beam intensity profile measurements using a Shack–Hartmann wavefront sensor for the (a) reference beam and (b) measurement beam. The intensity is normalized from one to $1/e^2$, which is the outer edge of each beam.

Table 2. The coefficient for the first 15 Zernike polynomials for reference and measurement beams (unit: micrometers).

Reference beam			Measurement beam		
Z_2	−0.706	Z_9	0.443	Z_2	−0.606
Z_3	−0.599	Z_{10}	0.277	Z_3	−0.681
Z_4	0.350	Z_{11}	0.268	Z_4	−0.152
Z_5	0.373	Z_{12}	0.081	Z_5	−0.066
Z_6	−0.383	Z_{13}	0.217	Z_6	−0.153
Z_7	−0.284	Z_{14}	−0.041	Z_7	−0.099
Z_8	0.499	Z_{15}	0.005	Z_8	0.419
				Z_9	0.477
				Z_{10}	0.207
				Z_{11}	0.148
				Z_{12}	−0.028
				Z_{13}	0.010
				Z_{14}	−0.018
				Z_{15}	−0.005

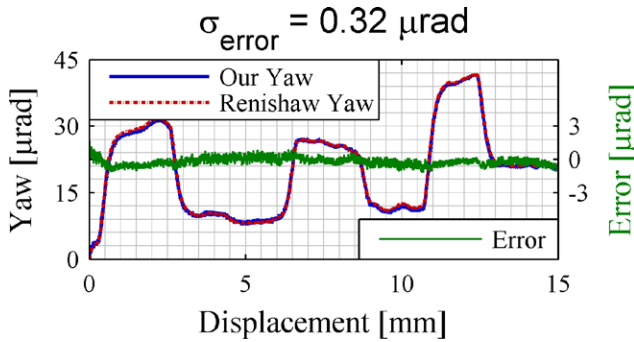


Figure 13. The comparison of yaw measurement during linear motion within 15 mm range processed using a simulated effective length 2.383 mm based on measured beam diameter, alignment errors and aberrations.

move between different setups. In this process, we assume the Renishaw system is the standard and inversely calculate the optimal equivalent length to best fit the two measurement results. The empirical calibrated equivalent length is 2.3587 mm and the comparison is shown in figure 14. The equivalent length calculated from our numerical simulation only has about a 1% difference compared to our empirically calibrated value. There are several factors that contribute to the difference. First, the beam profile is not exactly a Gaussian beam as we assume in the simulation. Secondly, there is a refractive index difference between two sides and the sensitivity to refractive index error is different for the two measurement systems. Finally, the measured dynamics for our 12 mm mirror target are slightly different compared to the 70 mm by 30 mm by 30 mm retroreflector target used by the Renishaw system, which results in slightly different responses when the stage is moving.

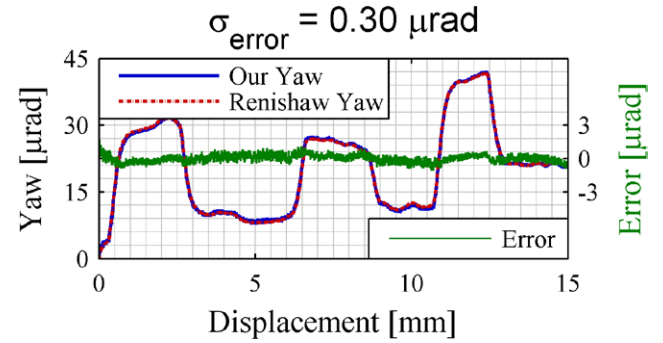


Figure 14. The comparison of yaw measurement during linear motion within 15 mm range processed using an empirical calibrated effective length 2.3587 mm.

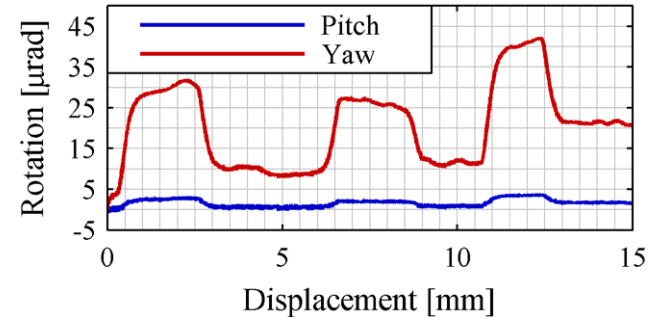


Figure 15. The pitch and yaw measurement results for linear stage within a 15 mm moving range.

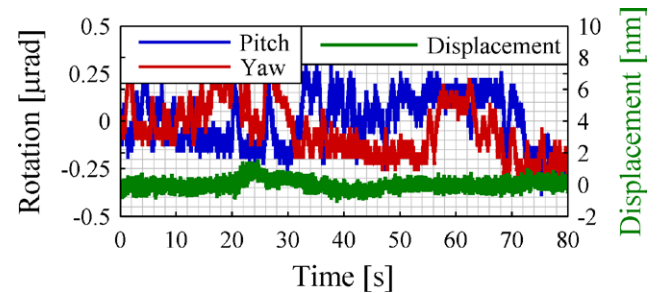


Figure 16. The noise floor measurements for pitch, yaw and displacement over 80 s for our three DOF interferometer. The variations are largely due to refractive index fluctuations.

After determining the equivalent length, the three DOF interferometer can then be used to calibrate the stage. Figure 15 shows the pitch and yaw measurement result for linear stage moving from 0 to 15 mm, which demonstrates that

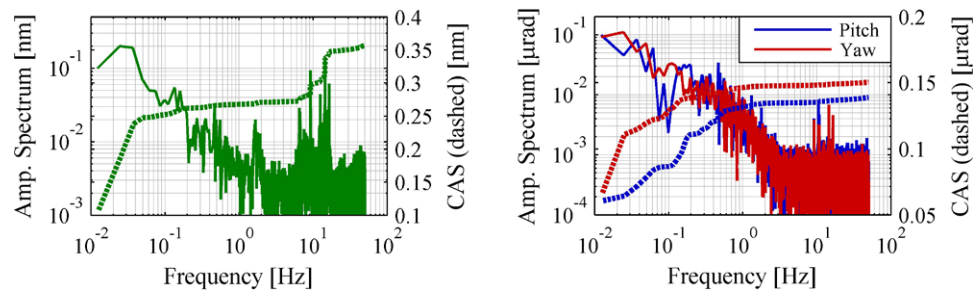


Figure 17. (a) Fourier spectrum and cumulative amplitude spectrum (CAS) of the displacement noise, demonstrating <0.4 nm of displacement noise. (b) Fourier spectrum and CAS of the pitch and yaw noise floors, demonstrating <0.2 μ rad of angular noise.

our interferometer can measure displacement, pitch and yaw simultaneously using a single beam and a small mirror target.

The noise floor over 80 s is shown in figure 16 at 100 Hz sampling frequency. A constant linear drift of approximately 8 nm was evident when the stage held at a constant position. Thus, the data shown in figure 16 shows the detrended Z-displacement noise floor. The variations in angle are assumed largely from spatial refractive index variations. The measurement limit for refractive index fluctuations is 10^{-8} , which over an optical path length of 100 mm yields a potential of 1 nm differences between quadrants on the photodiode. Given that the equivalent length is about ~ 2.5 mm, the expected angular change from refractive index is about 400 nrad. Thus, we are unable to distinguish angular errors from refractive index as opposed to other potential sources. In addition, a Fourier spectrum of the measurement noise and the cumulative amplitude spectrum (CAS), which shows an integration of the noise over the frequency regime indicating contributions from discrete frequencies, are shown in figure 17. It indicates that our displacement resolution is 0.4 nm and rotation resolution is 0.2 μ rad. This measurement resolution can be further increased through calibration in a better controlled measurement environment.

8. Conclusions

The basic form of differential wavefront sensing analytical models are based on the nominal beam size and detector size for fundamental order Gaussian beams and perform to within 10% of the target mirror angle change. A model for determining a more accurate equivalent length and linear range for metrology systems using DWS has been presented. Numerical simulations were performed to investigate the effects of beam size, detector size, different alignment errors, and aberrations for the DWS signals. For the initial alignment effects, the DWS signal sensitivity is approximately 10 times higher for beam size mismatch than for beam center mismatch. Furthermore, as our results demonstrate, incorporating alignment effects and beam aberrations into the Gaussian beam model improves the accuracy to $<1\%$, which is a $10 \times$ improvement over previously reported DWS results. The fiber-coupled three DOF interferometer we present in this manuscript has demonstrated calibrating a linear stage for displacement, pitch, and yaw simultaneously and can achieve a 0.4 nm linear noise floor and

a 0.2 μ rad angular noise floor. The yaw measurements agreed with a commercial angle interferometer to within 0.32 μ rad.

Compared with other multi-DOF sensing methods which combine a laser interferometer for linear displacement and autocollimation for angular displacement, our fiber-coupled three DOF interferometer uses less optical components and detectors, which makes the system more simple, compact and cost efficient. The resolution of our angular measurement is eight times higher than the previous work [30] using autocollimation for angular measurement. Finally, our angular sensitivity can be accurately predicted based on the proposed methodology and is in high agreement with the calibrated result.

Acknowledgments

The authors would like to acknowledge the support of the US Department of Commerce, National Institute of Standards and Technology under Award No. 70NANB12H186 and Award No. 70NANB14H266 and the National Science Foundation, under Awards CMMI:1265824 and IIP:1417032. The authors would like to thank Dr. Shane Woody at InSituTec, Inc. for fruitful discussions regarding this research and their STTR partnership.

References

- [1] Bobroff N 1993 Recent advances in displacement measuring interferometry *Meas. Sci. Technol.* **4** 907
- [2] Bosse H and Wilkening G 2005 Developments at PTB in nanometrology for support of the semiconductor industry *Meas. Sci. Technol.* **16** 2155
- [3] Tyler Estler W 1985 High-accuracy displacement interferometry refin air *Appl. Opt.* **24** 808–15
- [4] Haitjema H 2008 Achieving traceability and sub-nanometer uncertainty using interferometric techniques *Meas. Sci. Technol.* **19** 084002
- [5] Wu C-m, Lawall J and Deslattes R D 1999 Heterodyne interferometer with subatomic periodic nonlinearity *Appl. Opt.* **38** 4089–94
- [6] Lawall J and Kessler E 2000 Michelson interferometry with 10 pm accuracy *Rev. Sci. Instrum.* **71** 2669–76
- [7] Kim H S, Schmitz T L, Beckwith J F and Rueff M C 2008 A new heterodyne interferometer with zero periodic error and tunable beat frequency *Proc. 23rd American Society of Precision Engineering (ASPE) (Portland, Oregon)*

- [8] Joo K-N, Ellis J D, Spronck J W, van Kan P J and Schmidt R H M 2009 Simple heterodyne laser interferometer with subnanometer periodic errors *Opt. Lett.* **34** 386–8
- [9] Joo K-N, Ellis J D, Buice E S, Spronck J W and Schmidt R H M 2010 High resolution heterodyne interferometer without detectable periodic nonlinearity *Opt. Express* **18** 1159–65
- [10] Ellis J D, Meskers A J, Spronck J W and Schmidt R H M 2011 Fiber-coupled displacement interferometry without periodic nonlinearity *Opt. Lett.* **36** 3584–6
- [11] Chiu M-H and Su D-C 1997 Angle measurement using total-internal-reflection heterodyne interferometry *Opt. Eng.* **36** 1750–3
- [12] Zhou W and Cai L 1998 Interferometer for small-angle measurement based on total internal reflection *Appl. Opt.* **37** 5957–63
- [13] Marzolf J G 1964 Angle measuring interferometer *Rev. Sci. Instrum.* **35** 1212–5
- [14] Malacara D and Harris O 1970 Interferometric measurement of angles *Appl. Opt.* **9** 1630–3
- [15] Shi P and Stijns E 1993 Improving the linearity of the Michelson interferometric angular measurement by a parameter compensation method *Appl. Opt.* **32** 44–51
- [16] Morrison E, Meers B J, Robertson D I and Ward H 1994 Experimental demonstration of an automatic alignment system for optical interferometers *Appl. Opt.* **33** 5037–40
- [17] Morrison E, Meers B J, Robertson D I and Ward H 1994 Automatic alignment of optical interferometers *Appl. Opt.* **33** 5041–9
- [18] Heinzel G, Rüdiger A, Schilling R, Strain K, Winkler W, Mizuno J and Danzmann K 1999 Automatic beam alignment in the Garching 30-m prototype of a laser-interferometric gravitational wave detector *Opt. Commun.* **160** 321–34
- [19] Grote H, Heinzel G, Freise A, Gossler S, Willke B, Lück H, Ward H, Casey M M, Strain K A and Robertson D 2004 Alignment control of GEO 600 *Class. Quantum Grav.* **21** S441
- [20] Heinzel G, Wand V, Garcia A, Jennrich O, Braxmaier C, Robertson D, Middleton K, Hoyland D, Rüdiger A and Schilling R 2004 The LTP interferometer and phasemeter *Class. Quantum Grav.* **21** S581
- [21] Schuldt T, Gohlke M, Weise D, Johann U, Peters A and Braxmaier C 2009 Picometer and nanoradian optical heterodyne interferometry for translation and tilt metrology of the LISA gravitational reference sensor *Class. Quantum Grav.* **26** 085008
- [22] Audley H, Danzmann K, Marín A G, Heinzel G, Monsky A, Nofrarias M, Steier F, Gerardi D, Gerndt R and Hechenblaikner G 2011 The LISA Pathfinder interferometry—hardware and system testing *Class. Quantum Grav.* **28** 094003
- [23] Robertson D, Fitzsimons E, Killow C, Perreux-Lloyd M, Ward H, Bryant J, Cruise A, Dixon G, Hoyland D and Smith D 2013 Construction and testing of the optical bench for LISA Pathfinder *Class. Quantum Grav.* **30** 085006
- [24] Heinzel G, Braxmaier C, Schilling R, Rüdiger A, Robertson D, Te Plate M, Wand V, Arai K, Johann U and Danzmann K 2003 Interferometry for the LISA technology package (LTP) aboard SMART-2 *Class. Quantum Grav.* **20** S153
- [25] Hechenblaikner G, Gerndt R, Johann U, Luetzow-Wentzky P, Wand V, Audley H, Danzmann K, Garcia-Marín A, Heinzel G and Nofrarias M 2010 Coupling characterization and noise studies of the optical metrology system onboard the LISA Pathfinder mission *Appl. Opt.* **49** 5665–77
- [26] Hechenblaikner G 2010 Measurement of the absolute wavefront curvature radius in a heterodyne interferometer *J. Opt. Soc. Am. A* **27** 2078–83
- [27] Wanner G, Heinzel G, Kochkina E, Mahrtdt C, Sheard B S, Schuster S and Danzmann K 2012 Methods for simulating the readout of lengths and angles in laser interferometers with Gaussian beams *Opt. Commun.* **285** 4831–9
- [28] Lee S W, Mayor R and Ni J 2005 Development of a six-degree-of-freedom geometric error measurement system for a meso-scale machine tool *J. Manuf. Sci. Eng.* **127** 857–65
- [29] Lee C, Kim G H and Lee S-K 2011 Design and construction of a single unit multi-function optical encoder for a six-degree-of-freedom motion error measurement in an ultraprecision linear stage *Meas. Sci. Technol.* **22** 105901
- [30] Qibo F, Bin Z, Cunxing C, Cuifang K, Yusheng Z and Fenglin Y 2013 Development of a simple system for simultaneously measuring 6DOF geometric motion errors of a linear guide *Opt. Express* **21** 25805–19
- [31] Hsieh H-L and Pan S-W 2015 Development of a grating-based interferometer for six-degree-of-freedom displacement and angle measurements *Opt. Express* **23** 2451–65
- [32] Gillmer S R, Smith R C G, Woody S C and Ellis J D 2014 Compact fiber-coupled three degree-of-freedom displacement interferometry for nanopositioning stage calibration *Meas. Sci. Technol.* **25** 075205
- [33] Ellis J D 2014 *Field Guide to Displacement Measuring Interferometry* (Bellingham, WA: SPIE Optical Engineering Press)
- [34] Mahajan V N and Shannon R R 1994 Zernike circle polynomials and optical aberrations of systems with circular pupils *Appl. Opt.* **33** 8121–4